AGU PUBLICATIONS

JGR

Journal of Geophysical Research: Atmospheres

RESEARCH ARTICLE

10.1002/2014JD022077

Key Points:
- Atmospheric dust radiative effect is measured using space and ground instruments
- Daytime cycle of radiative effect analysed at TOA, surface, and in the atmosphere
- Dust atmospheric radiative heating is dominated by the surface SW cooling effect

Correspondence to:
J. R. Banks,
j.banks@imperial.ac.uk

Citation:
Banks, J. R., H. E. Brindley, M. Hobby, and J. H. Marsham (2014), The daytime cycle in dust aerosol direct radiative effects observed in the central Sahara during the Fennec campaign in June 2011, *J. Geophys. Res. Atmos.*, *119*, 13,861–13,876, doi:10.1002/2014JD022077.

Received 23 MAY 2014
Accepted 18 NOV 2014
Accepted article online 24 NOV 2014
Published online 16 DEC 2014

The daytime cycle in dust aerosol direct radiative effects observed in the central Sahara during the Fennec campaign in June 2011

Jamie R. Banks[1], Helen E. Brindley[1], Matthew Hobby[2], and John H. Marsham[2]

[1]Space and Atmospheric Physics Group, Imperial College, London, UK, [2]School of Earth and Environment, University of Leeds, Leeds, UK

Abstract The direct clear-sky radiative effect (DRE) of atmospheric mineral dust is diagnosed over the Bordj Badji Mokhtar (BBM) supersite in the central Sahara during the Fennec campaign in June 2011. During this period, thick dust events were observed, with aerosol optical depth values peaking at 3.5. Satellite observations from Meteosat-9 are combined with ground-based radiative flux measurements to obtain estimates of DRE at the surface, top-of-atmosphere (TOA), and within the atmosphere. At TOA, there is a distinct daytime cycle in net DRE. Both shortwave (SW) and longwave (LW) DRE peak around noon and induce a warming of the Earth-atmosphere system. Toward dusk and dawn, the LW DRE reduces while the SW effect can switch sign triggering net radiative cooling. The net TOA DRE mean values range from $-9\,\mathrm{W\,m^{-2}}$ in the morning to heating of $+59\,\mathrm{W\,m^{-2}}$ near midday. At the surface, the SW dust impact is larger than at TOA: SW scattering and absorption by dust results in a mean surface radiative cooling of $145\,\mathrm{W\,m^{-2}}$. The corresponding mean surface heating caused by increased downward LW emission from the dust layer is a factor of 6 smaller. The dust impact on the magnitude and variability of the atmospheric radiative divergence is dominated by the SW cooling of the surface, modified by the smaller SW and LW effects at TOA. Consequently, dust has a mean daytime net radiative warming effect on the atmosphere of $153\,\mathrm{W\,m^{-2}}$.

1. Introduction

It has been known for some time that mineral dust aerosol can exert a substantial impact on radiative fluxes at the top of the Earth's atmosphere (TOA), at the surface, and within the atmosphere itself [e.g., *Hsu et al.*, 2000; *Quijano et al.*, 2000; *McFarlane et al.*, 2009]. The typical size distribution of dust particles means that significant radiative effects can be seen in both the shortwave (SW) and longwave (LW) parts of the electromagnetic spectrum [e.g., *Haywood et al.*, 2001; *Highwood et al.*, 2003]. Within Numerical Weather Prediction (NWP) models, it has been shown that the absence of an explicit representation of mineral dust can result in TOA LW flux biases of up to $50\,\mathrm{W\,m^{-2}}$ over north-western Africa [*Haywood et al.*, 2005]. A more recent study, comparing the output from an ensemble of climate models with observed TOA fluxes, indicates that similar model overestimates of clear-sky OLR (of the order $20\,\mathrm{W\,m^{-2}}$) are present over parts of the western Sahara during summer months [*Allan et al.*, 2011]. Similarly, detailed NWP comparisons with TOA reflected SW fluxes observed over Niamey, Niger, indicated a systematic model underestimate in cloud free conditions attributed partly to dust presence and partly to inadequacies in the model surface albedo [*Milton et al.*, 2008]. The same study used co-located ground-based observations to highlight significant model biases in corresponding surface fluxes, with the absence of aerosol in the model resulting in typical overestimates of the downwelling SW component of up to $50\,\mathrm{W\,m^{-2}}$. Over the site and period of study in question mineral dust aerosol contributed between 50 and 90% of the total aerosol loading. These effects are sufficiently large that improving the representation of dust radiative effects in NWP models can be shown to increase forecast skill [*Tompkins et al.*, 2005; *Rodwell and Jung*, 2008].

The West African Sahara as a whole is subject to some of the highest atmospheric dust loadings on the planet in boreal summer [e.g., *Engelstaedter et al.*, 2006] and part of the problem associated with improving model simulations over this region is the relative paucity of ground-based and in situ measurements with which to evaluate predictions. Due to the considerable difficulties in accessing the region, such observations as are available have tended to be made on the desert margins [e.g., *Slingo et al.*, 2009; *Ansmann et al.*, 2011; *Haywood et al.*, 2011]. The recent Fennec [*Washington et al.*, 2012] campaigns in June 2011 and June

2012 have provided a unique observational data set from the central Sahara from ground sites [*Marsham et al.*, 2013; *Todd et al.*, 2013; *Hobby et al.*, 2013] and aircraft [e.g., *Ryder et al.*, 2013a]. Linking this information with that available from satellite permits the derivation of the overall radiative effect of dust at the TOA, surface, and on the atmospheric column itself. In this paper we perform such an analysis, using radiative flux observations from Fennec supersite-1 at Bordj Badji Mokhtar (BBM) in south-west Algeria, together with geostationary satellite observations from Meteosat-9 to study the radiation environment in the central Sahara during June 2011. Dust loadings during the month were substantial with measured aerosol optical depths (AOD) ranging up to ~3.5, from a combination of emission mechanisms including cold pool outflows, low-level jets, and dry convective plumes [*Allen et al.*, 2013]. The insights gained are of interest in their own right, but we anticipate that they will also be used in the future to assess model performance over the site.

Previous studies have indicated that dust activity over the Sahara as a whole has a distinct dependence on time of day [e.g., *Schepanski et al.*, 2009] linked to the characteristic timing of several of the key mechanisms responsible for uplift [e.g., *Knippertz and Todd*, 2012, and references therein]. During June 2011, over BBM itself, *Marsham et al.* [2013] found that dust uplift is split relatively equally between day and night and that around 50% of uplift is associated with cold pool outflow from moist convection (haboobs). *Allen et al.* [2013] confirm these findings and also suggest that dust clouds transported by haboobs over BBM tend to consist of larger particles and have higher optical depths than those uplifted locally (consistent with *Ryder et al.* [2013b]). Once uplifted, dust is mixed upward through the Saharan boundary layer by dry convection, reaching around 2 km at midday and 5–6 km by 1800 UTC. *Marsham et al.* [2013] show that, consistent with previous case studies [*Marsham et al.*, 2008; *BouKaram et al.*, 2008], dust is associated with moist monsoon air at BBM in June 2011. Dust and cloud are therefore associated and may have similar effects on the net surface radiative heating.

Not only does dust activity have a dependence on time of day but so too does the dust radiative effect for a given dust loading. Observations from geostationary satellites can be used to investigate this behavior. For example, analysis has been carried out using measurements taken from the GOES 8 satellite during the Puerto Rico Dust Experiment (PRIDE) in July 2000 [*Wang et al.*, 2003], in conjunction with ground-based radiative flux measurements. This work showed that aerosol effects on SW fluxes would be misrepresented if daily mean aerosol optical thicknesses (rather than instantaneous values) were used in radiative transfer calculations to derive the aerosol radiative effects, by 4 W m^{-2} at the surface and 2 W m^{-2} at TOA [*Christopher et al.*, 2003]. Meanwhile over the Sahara measurements from Meteosat-9 have been used to quantify direct clear-sky dust radiative effects at TOA [*Ansell et al.*, 2014] during the GERBILS field campaign [*Haywood et al.*, 2011].

The major goal of this study is to understand and to quantify the dust direct clear-sky radiative effect at the surface, within the atmosphere and at TOA, throughout the day, exploiting the high temporal resolution sampling available from the surface and satellite observations. A secondary goal is to probe whether these dust radiative impacts have any coherent subdaily signature and what the implications of this may be for records derived from instruments in Low Earth Orbit which may only be able to sample at specific times of day.

2. Data and Methodology

2.1. Satellite Measurements From Meteosat-9

In this paper we use observations from the Spinning Enhanced Visible and InfraRed Imager (SEVIRI) and Geostationary Earth Radiation Budget (GERB) instruments on Meteosat-9. In geostationary orbit above the equatorial Atlantic, SEVIRI provides observations every 15 min of Africa and much of Europe and the Middle East, at a horizontal resolution of 3×3 km at nadir [*Schmetz et al.*, 2002]. Previous studies [*Brindley and Russell*, 2009; *Banks and Brindley*, 2013] have developed and evaluated a retrieval method using SEVIRI to quantify mineral dust aerosol optical depth (AOD) over the Sahara, at a wavelength of 550 nm. The method is currently restricted to sunlit hours, in cloud-free conditions, with a solar zenith angle cutoff of 70°, so for this study AOD retrievals from SEVIRI between 0700 and 1630 UTC were available. Previous work [*Banks et al.*, 2013] shows that this retrieval is particularly effective at quantifying heavy dust loadings but is typically biased high against other ground-based and satellite products when the dust loading is low. Against ground-based AERONET [*Holben et al.*, 1998] measurements from several sites across North Africa in June

2011, the SEVIRI retrievals have been shown to have an AOD bias of +0.11. The SEVIRI retrievals are also sensitive to atmospheric column moisture and are less effective in cooler conditions especially during winter [*Banks and Brindley*, 2013].

The net dust direct radiative effect (DRE) at the TOA is a measure of the overall perturbation of the Earth's radiation budget due to the presence of dust. High temporal resolution TOA shortwave (SW, covering the range 0.32–4 μm) and longwave (LW, covering the range 4–100 μm) fluxes are available from the GERB instrument also on Meteosat-9 [*Harries et al.*, 2005]. For our purposes here, we use GERB High Resolution (HR) fluxes [*Dewitte et al.*, 2008], which are produced using a narrow-broad band conversion of SEVIRI radiance measurements, subsequently scaled by co-located GERB measurements and converted into broadband flux measurements at a horizontal resolution of 3×3 SEVIRI pixels. This enhances the native GERB spatial resolution of ~45 to ~9 km at nadir.

Uncertainties on the GERB HR fluxes arise from uncertainties in the radiance measurements and also from uncertainties in the radiance-to-flux conversion. For the latter the choice of Angular Distribution Model (ADM) is vital: in the SW they are used as proposed by *Loeb et al.* [2003], whereby scenes are classified as clear or cloudy; in the LW the GERB HR fluxes are produced following *Clerbaux et al.* [2003]. Explicit aerosol models are not included in these calculations. Based on long-term comparisons with ground-based measurements, *Slingo et al.* [2006] propose total uncertainties of 10 W m^{-2} in the SW fluxes, and 5 W m^{-2} in the LW, although they do note that these errors may be larger in the presence of aerosol due to the ADMs used. A more conservative estimate is made by *Ansell et al.* [2014], based on long-term comparisons with CERES (Clouds and the Earth's Radiant Energy System) flux data, independent measurements from a different platform [*Wielicki et al.*, 1996]. They suggest an upper estimate of an uncertainty of 10% in the GERB fluxes in both bands.

The calculation of the TOA SW DRE (DRE_{SWTOA}) is a two-step process and is described in detail by *Ansell et al.* [2014]. First, since surface albedo has a solar zenith angle dependence [*Wang et al.*, 2005], the pristine-sky planetary albedo is calculated for each timeslot in the daily cycle from a linear regression of the SEVIRI AOD against albedo for all HR pixels within a 0.25° grid cell. To minimise nonlinear effects on the measured instantaneous planetary albedo due to dust, measurements when the SEVIRI AOD is greater than 0.5 are excluded, as are regressions with an AOD range of less than 0.15. If such conditions are not met, then the pristine-sky albedo is derived by calculating the average of the retrieved pristine-sky albedoes for other grid cells in the Saharan domain which have similar (within a bin size of 5%) climatological reflectances at 600 nm as derived from SEVIRI [*Derrien and Gléau*, 2005]. For information, over the period considered, this results in a minimum pristine-sky albedo occurring at 1200 UTC of 0.295 and a maximum albedo at 0700 UTC of 0.354. Second, the instantaneous DRE is calculated by subtracting the measured TOA SW flux from the pristine-sky flux, calculated by multiplying the incoming SW flux by the derived pristine-sky planetary albedo. Note that in common with the other DRE estimates made here, instantaneous DRE_{SWTOA} retrievals are only calculated for cloud-free timeslots when SEVIRI AOD retrievals are available.

The TOA LW DRE (DRE_{LWTOA}) is calculated using a 28 day rolling-window pristine-sky reference method (described in detail by *Brindley* [2007] and *Brindley and Russell* [2009]) to identify the pristine-sky TOA LW flux for each timeslot and HR pixel, taking into account variations in the skin temperature and upper and lower tropospheric humidities. The ECMWF ERA-Interim reanalysis data set [*Dee et al.*, 2011] is used to define the skin temperature and tropospheric humidity values. The pristine-sky days for each timeslot in the daily cycle are identified by finding the day with the minimum difference between the brightness temperature at 10.8 μm and simulated brightness temperatures derived from the ERA-Interim values of skin temperature and column water vapor [*Brindley*, 2007; *Brindley and Russell*, 2009]. It is thus possible for a different day to be identified as pristine at each time-slot. For each timeslot, a correction is made to the TOA LW flux observed on the pristine-day to account for the impact of variations in temperature and humidity between this day and that of the actual aerosol observation. In this way we obtain a pristine-sky TOA LW flux appropriate to the meteorological conditions on the aerosol-contaminated day. *Brindley* [2007] discusses the effect of typical uncertainties in skin temperature and humidity profile on the estimation of pristine-sky TOA LW flux and suggests an uncertainty of ~5 W m^{-2}. Instantaneous TOA LW fluxes in the presence of dust are then subtracted from the appropriate pristine-sky values. Note however that the tropospheric humidity may be underestimated in the presence of haboobs, since these are essentially missing from models with parameterised convection [*Garcia-Carreras et al.*, 2013; *Marsham et al.*, 2011]. This may lead to additional

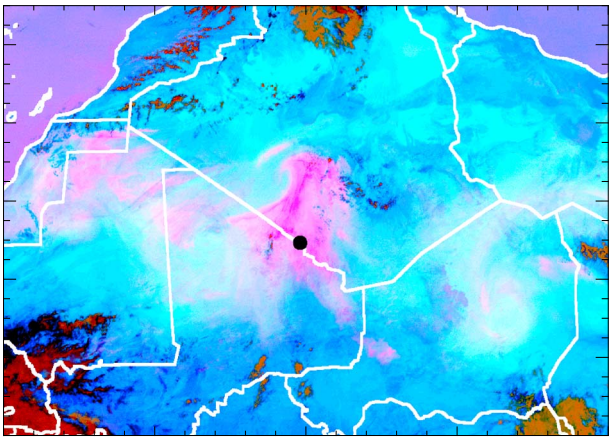

Figure 1. "Desert-dust" RGB composite image [*Lensky and Rosenfeld*, 2008] from SEVIRI at 1300 UTC on 21 June 2011. BBM is marked as a black dot, on the Algerian/Malian border. Dust is marked as pink, while the desert surface appears bright blue. For this time the BBM AERONET Level 2 AOD at 550 nm is 3.5, while the SEVIRI retrieved AOD is 2.8. The instantaneous SW and LW TOA DREs over BBM are 13 and 53 W m^{-2}, respectively.

uncertainties in the derivation of the pristine-sky flux, although the assimilation of 3- to 6-hourly Fennec radiosondes reduces this error for the time period we consider here.

Hence, in the SW,

$$DRE_{\mathrm{SWTOA}} = SW_{\mathrm{TOApris}} - SW_{\mathrm{TOA}}, \quad (1)$$

with a similar equation holding for DRE_{LWTOA}. In this way a positive TOA DRE value is indicative of a warming of the overall Earth-atmosphere system. Uncertainties in the instantaneous estimates of DRE_{SWTOA} and DRE_{LWTOA} are ~15 W m^{-2} and ~10 W m^{-2}, respectively [*Ansell et al.*, 2014]. These estimates include the effects of the uncertainty in the estimation of the pristine-sky fluxes.

2.2. Ground-Based Data From the Bordj Badji Mokhtar Fennec Supersite-1

As part of the Fennec project, the BBM supersite in the Algerian Sahara (21.38°N, 0.92°E) was established in order to produce the first comprehensive in situ data set of dust and meteorology at an observing site in the central Sahara [*Marsham et al.*, 2013]. This site is particularly well placed to observe some of the most frequent thick dust storms in the Sahara [e.g., *Prospero et al.*, 2002; *Ashpole and Washington*, 2012], an example image from SEVIRI of dust activity over this region is presented in Figure 1. Instrumentation included a Cimel sun-photometer for measurements of AOD and aerosol properties, 3- to 6-hourly radiosonde launches, and a 2 m high mast holding a Kipp & Zonen CNR4 radiometer for measurements of upwelling and downwelling radiative fluxes in the SW and LW (part of the "flux-tower," henceforth denoted FT). The SW is measured in the range 0.3–2.8 μm, while the LW is measured between 4.5 and 42 μm: these ranges are different to those of GERB, and these are a potential source of uncertainty when comparing and combining the two measurement sources. The FT data have a temporal resolution of 1 s. The systematic uncertainty on the instantaneous flux measurements, quoted by the manufacturer is 3.5% [*Hobby et al.*, 2013]; however, night-time SW flux measurements suggest that any bias is less than 2 W m^{-2}. Data from the FT also include measurements of 2 m air temperature, relative humidity, and pressure. The sun-photometer is part of the AERONET program [*Holben et al.*, 1998] and level-2 cloud-screened and quality-assured data are used in this study, as an independent but co-located measure of the dust loading for comparison and validation purposes, complementary to the SEVIRI AODs. For consistency between the various data sources, the FT and AERONET data are averaged to half-hourly temporal resolution, and, given the availability of each source, the period of study covers 20 days, between 9 and 28 June. On all of these days, all of the AERONET observations are classified as dusty using criteria based on the Ångström coefficient and the AOD at 1020 nm as proposed by *Dubovik et al.* [2002]. The Level 2 AERONET Ångström coefficient data range from −0.07 to 0.44, typical of desert dust. This is much too low for the aerosol to have been emitted by biomass burning or to have an urban/industrial source, nor could the aerosol be of maritime origin given BBM's inland location more than 1000 km from the ocean. Hence, we infer that the dominant aerosol above BBM is desert dust.

At the surface, we derive the surface dust SW DRE (DRE_{SWSFC}) by referencing the instantaneous upwelling and downwelling fluxes to the corresponding pristine-sky values:

$$DRE_{\mathrm{SWSFC}} = \left(SW_{\mathrm{sfcd}} - SW_{\mathrm{sfcu}}\right)_{\mathrm{inst}} - \left(SW_{\mathrm{sfcd}} - SW_{\mathrm{sfcu}}\right)_{\mathrm{prist}}, \quad (2)$$

where "prist" indicates pristine-sky values, "inst" instantaneous values, and d/u the downwelling/upwelling component of each. The convention used means that a positive DRE value is indicative of a dust induced surface SW radiative warming. The pristine-sky values of SW_{sfcd} for each timeslot are estimated using the

SBDART radiative transfer code [*Ricchiazzi et al.*, 1998], using atmospheric profiles over BBM from radiosonde measurements. For ozone profiles, and to fill in altitude layers above the radiosonde atmospheric profiles, we use ECMWF ERA-Interim Re-Analysis data.

In the SW, dust scatters and absorbs solar radiation: this instantaneously reduces SW_{sfcd}. In the LW, dust absorbs and emits radiation, instantaneously increasing LW_{sfcd}. Over time, both perturbations affect the surface temperature but there is no instantaneous effect on LW_{sfcu}. Hence, in calculating DRE_{LWSFC}, we only consider the downwelling component in equation 2. Here the pristine-sky LW_{sfcd} values are estimated using the MODTRAN4 radiative transfer code [*Anderson et al.*, 2000], again using radiosonde and ERA-Interim Re-Analysis data as input. The broadband emissivity of the surface at BBM is 0.88±0.01 as calculated following the method of *Ogawa et al.* [2008] using MODerate resolution Imaging Spectroradiometer (MODIS) spectral emissivity data for June 2011. For both SW and LW simulations, the spectral range considered matches that of the relevant FT instrument.

Using a combination of GERB and FT data, the atmospheric radiative heating can be quantified by calculating the atmospheric radiative divergence. We take the convention that a positive value is indicative of atmospheric radiative heating, so in the SW

$$SW_{div} = SW_{in} - SW_{TOA} - SW_{sfcd} + SW_{sfcu}, \tag{3}$$

where "in" refers to the incoming solar flux at the TOA, "TOA" the reflected SW flux derived from the GERB HR fluxes, and "sfc-d/u" the downwelling/upwelling SW flux at the surface, respectively. A similar equation can be formed for the LW radiative divergence, removing the incoming term. Note that, as written, in this equation there is no attempt to separate out the radiative effect of dust from that of other components, such as water vapor and clouds.

The difference in the spectral range covered by GERB at the TOA, and the FT at the surface has the potential to introduce systematic biases into the radiative divergence estimates. To assess this possibility, we utilize the pristine-sky simulations described above, comparing the fluxes integrated over the GERB spectral range to those over the more limited FT coverage. For SW surface fluxes, these suggest that we would expect a systematic low bias of ~0.5%, which translates to a reduction in SW_{sfcd} of ~5 W m^{-2} at peak solar insolation. Given the surface albedo, a corresponding reduction of ~1.5 W m^{-2} in SW_{sfcu} would be seen. Since the biases act in opposite directions in terms of their contribution to the SW radiative divergence, the maximum bias that would be expected is ~ +3.5 W m^{-2}.

In the LW, although the restricted wavelength range of the FT has a markedly reduced LW_{sfcu} (of the order 25 W m^{-2}), most of this reduction occurs at wavelengths > 42 μm. In this part of the spectrum, the lower atmosphere effectively acts as a blackbody radiating at a temperature similar to that of the surface such that a similar reduction is also seen in LW_{sfcd}. Hence, the overall impact on the net LW surface flux is substantially reduced, resulting in a bias in LW radiative divergence that ranges between −0.6 and −3.8 W m^{-2}.

Note that in both cases the estimates of the impact of the change in spectral range have been made using pristine-sky simulations. In the LW, because of the opacity of the atmosphere at the missing longer wavelengths, and the small amount of energy at the missing shorter wavelengths, a similar conclusion would be expected under dusty or cloudy conditions. For the SW, it is possible that the presence of cloud or dust aerosol will change the spectral distribution of energy incident at the surface such that a greater proportion of the total radiation is seen at longer wavelengths. However, in both cases the total amount of incident flux will reduce such that we would expect the absolute bias caused by the difference in spectral range to be smaller than that quoted above.

Finally, by combining equations 1 and 2, we can estimate the dust-only effect on atmospheric radiative divergence as, in the SW,

$$SW_{divdust} = DRE_{SWTOA} - DRE_{SWSFC}, \tag{4}$$

where a positive value indicates atmospheric heating, with an analogous equation holding for the dust only LW radiative divergence.

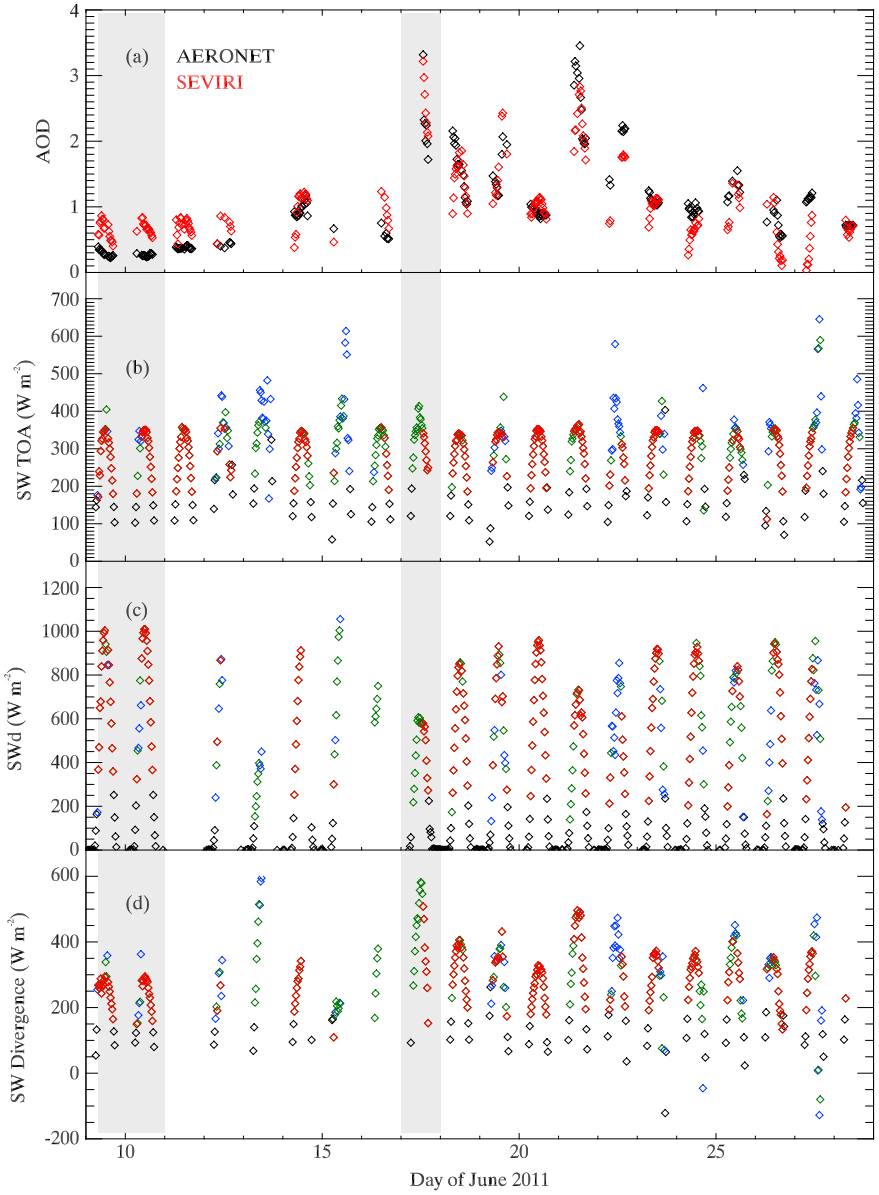

Figure 2. Half-hourly timeseries of (a) AOD at 550 nm from AERONET and SEVIRI, (b) SW TOA flux, (c) SW surface downwelling flux, and (d) SW radiative flux divergence. Colors in Figures 2b–2d indicate various regimes of cloud and night: black indicates night and twilight measurements (1700–0630 UTC, i.e., 58.3% of measurements), blue indicates daytime points when neither AERONET nor SEVIRI made a retrieval (8.4%), likely due to cloud, red indicates when they both did (22.0%), and green indicates when one but not the other did (11.3%); this may imply drifting cloud or very thick dust. Grey shading indicates selected light and heavy dust days.

3. Results

3.1. Atmospheric Fluxes and Divergences

Figures 2b–2d present timeseries of the observed outgoing fluxes at the TOA (Figure 2b), downwelling fluxes at the surface (Figure 2c), and associated atmospheric radiative flux divergence (Figure 2d) for the SW component with analogous information provided in Figures 3b–3d for the LW. In both cases, Figure 3a presents a timeseries of the associated AODs from SEVIRI and AERONET (at 550 nm: for AERONET measurements, this is derived from the relationship between the optical depth at 675 nm and the Ångström coefficient [*Eck et al.*, 1999]) to provide an easy reference to dust presence. In Figures 3b–3d, points are color coded to reflect timings and atmospheric conditions. Black are timeslots between 1700 and 0630 UTC, when no SEVIRI retrievals are attempted, blue shows points between 0700 and 1630 UTC when neither SEVIRI nor

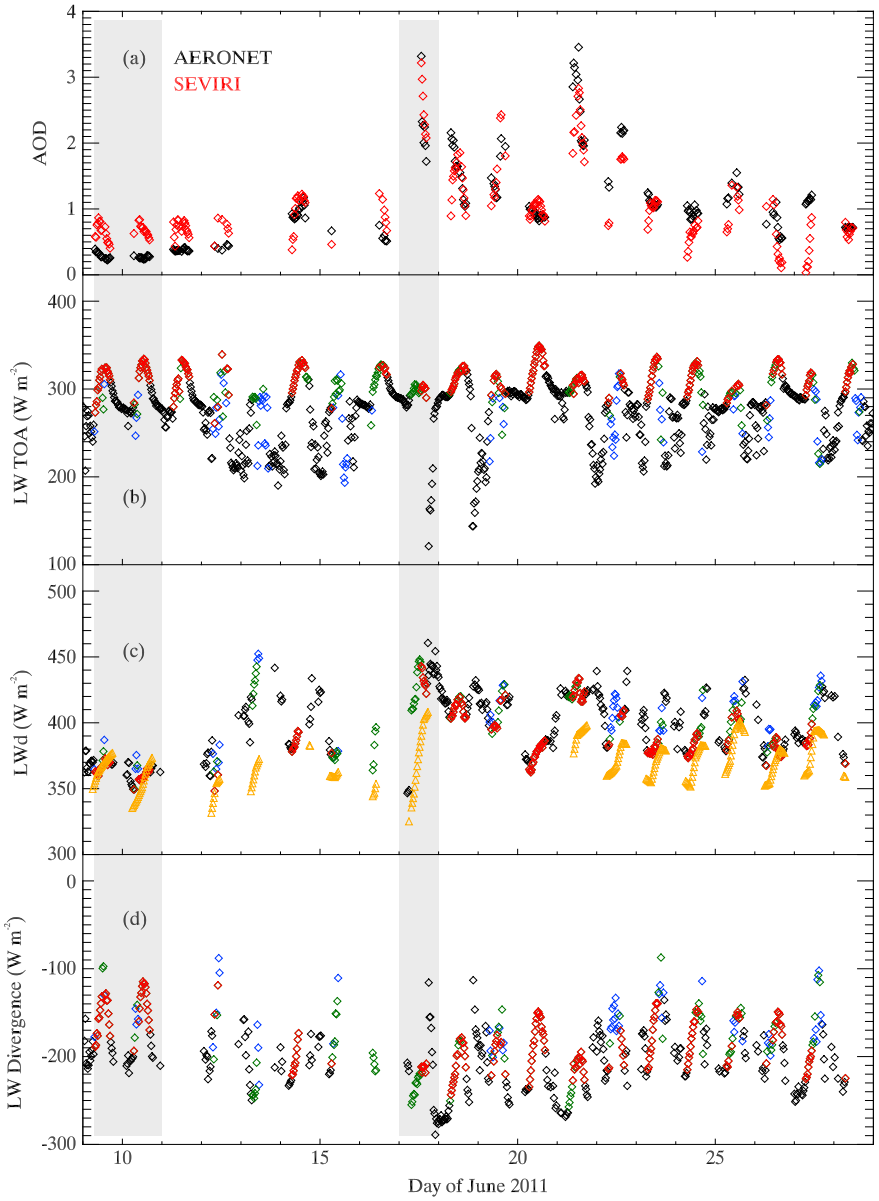

Figure 3. As in Figure 2, but for AODs and LW fluxes and divergences. The orange symbols in Figure 3c indicate the MODTRAN4-simulated pristine-sky downwelling LW flux at the surface.

AERONET indicate dust presence (implicitly indicating the presence of cloud), and red shows when both SEVIRI and AERONET indicate dust and green when one of the two instruments indicates dust. Gaps within the surface and atmospheric data indicate periods when the data were unavailable. For the subset of available co-located AERONET and SEVIRI retrievals the SEVIRI AOD and AERONET AOD products have a Pearson's correlation coefficient (r) of 0.83, the RMS difference between the data sets is 0.38, and SEVIRI's bias against the AERONET observations is −0.002. As discussed by *Marsham et al.* [2013], the period of 8–12 June is a dry and relatively dust-free period marked by northerly Harmattan winds, as opposed to the moist intrusions from the monsoon to the south that are seen more often in the mid to later stages of the month and which give rise to some of the most intense dust activity during which the AOD can exceed 3.

Turning to the radiative fluxes, as expected, in the SW there is a clear periodicity which follows the diurnal cycle of insolation and is seen at the TOA, within the atmosphere and at the surface. At the TOA, the presence of cloud tends to perturb the generic amplitude of the cycle, strongly enhancing the planetary albedo above the site (Figure 2b, blue points). Airborne dust is detected by either the ground based

sun-photometer or SEVIRI for approximately 80% of the daytime slots, while cloud is detected for the remaining 20%. For this site, at this time of year, dust presence is thus rather ubiquitous, but it is also true that at least for the satellite observations, its presence may be underestimated due to cloud screening effects. Certainly some of the points colored green in Figures 2b–2d appear to show consistency with measurements defined as "dusty" by both instruments at other times on the same day. Overall, there appears to be relatively little day-to-day variability in the reflected TOA SW fluxes in the presence of dust despite there being a marked variation in the dust optical depth (see Figure 2a): at 1200 UTC, for days when SEVIRI makes a successful retrieval, the mean reflected TOA SW flux is 365 W m^{-2} with an associated standard deviation of 8 W m^{-2}.

At the surface, the effect of day-to-day variability in atmospheric dust loading on the downward SW flux is more evident. For example, on 21 June, dust optical depths of up to 3.5 are recorded by AERONET (Figure 2a). At the TOA (Figure 2b), reflected SW fluxes show only marginal increases (12 W m^{-2} at midday, or +3%) compared to the equivalent values recorded in the less turbid conditions the day before (AOD∼1). In contrast, at midday the downward surface flux is reduced by ∼230 W m^{-2} (Figure 2c), a reduction of 24%. This differing sensitivity propagates through to the SW atmospheric radiative divergence with a strong increase in SW atmospheric heating seen under the heaviest dust loadings on 17 and 21 June (Figure 2d) from a typical low-dust value of ∼300 W m^{-2} to as much as ∼580 W m^{-2}. Although over a different location, these perturbations are of a similar order of magnitude to those reported by *Slingo et al.* [2006] in their study of an intense Saharan dust storm over a sub-Sahelian site.

A marked diurnal cycle is also evident in the timeseries of outgoing longwave radiation (OLR) through June (Figure 3). OLR increases rapidly from dawn onward, reaching a peak shortly after midday, before reducing more slowly as the afternoon progresses. As might be expected, the amplitude and coherence of the cycle is largest under lighter dust loadings due to the strong dependence of the signal on the daily cycle in surface temperature. The presence of high dust loading, cloud, or increased water vapor content, acts to disrupt this behavior by partially decoupling the surface from the TOA, reducing the amplitude of the OLR signal during sunlit hours and perturbing its periodic behavior (Figure 3b, e.g., 21 June compared to 20 June). At the surface, during sunlit hours enhanced atmospheric absorption by dust would be expected to result in an increase in downwelling LW radiation, and this is evident on 17 and 21 June. Although it cannot be confirmed from the measurements available here, the patterns in TOA and surface LW radiation would also suggest that either thick dust or cloud was present through the majority of nights from 17 June onward except 19 and 26 June, as marked by troughs in LW TOA fluxes below ∼270 W m^{-2} and, to a lesser extent, elevated nighttime values of LW SFC fluxes. This is consistent with the findings of *Marsham et al.* [2013], who carried out an overview of the June 2011 conditions at BBM, and manual inspection of SEVIRI imagery. The LW radiative divergence is always negative, indicating atmospheric radiative cooling. Comparison of days with high (e.g., 17 June) and low (e.g., 9 June) dust loadings, marked by grey shading in the figures, indicates that the increase in downward radiation to the surface is larger than the corresponding reduction in OLR, resulting in an enhanced atmospheric radiative cooling. However, it should be noted that variability in cloud, atmospheric water vapor content, and temperature will also influence the patterns seen in LW flux and radiative divergence, and also that dust is often associated with water vapor and cloud.

Figure 4 illustrates the overall net outgoing radiation at TOA, the net radiation down to the surface, and the net atmospheric radiative divergence obtained by combining the SW and LW components shown in Figures 2 and 3. Focusing particularly on the net divergence, the relative magnitudes of the signals have the consequence that when solar elevation exceeds ∼20–30° the SW component tends to dominate, resulting in atmospheric radiative warming. At lower elevations, the LW component becomes more significant and a small net cooling can result toward dusk and dawn. Through the night, obviously the LW component is all that contributes to the net such that the atmosphere cools radiatively.

3.2. Dust Impact

Having described the overall behavior of the SW and LW radiative fluxes and divergence, in this section we attempt to isolate the dust impact on these quantities. Figure 5 presents calculations of the dust DRE at the TOA and the surface and of the atmospheric radiative divergence due to dust derived from equation 4. To allow an easy comparison to the dust loading at any given time, the timeseries of AOD from AERONET and SEVIRI is once again provided in Figure 5a. Further to this, scatterplots of the dust DRE products with respect to SEVIRI AOD are plotted in Figure 6. For all points in this timeseries, the data are subset such that

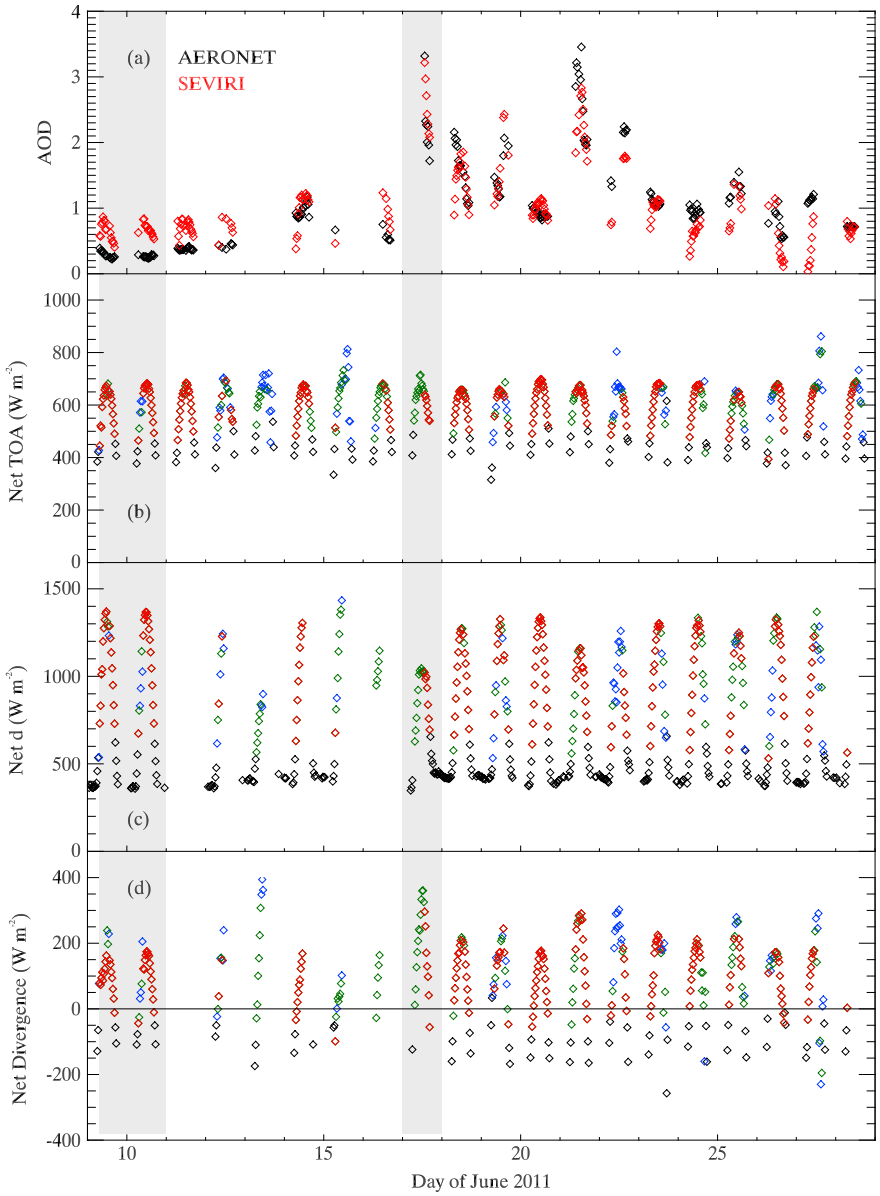

Figure 4. As in Figure 2, but for AODs and net fluxes and divergences.

there must be simultaneous successful measurements of AOD and DRE from orbit and of fluxes from the FT. Hence, only clear-sky conditions are analysed. This analysis will therefore miss any patterns in the cycle of dust activity and effects when cloud is present, such as during cold pool events which are a major trigger for dust storm uplift.

Reassuringly, Figure 6b shows that the DRE_{LWTOA} is highly correlated with the SEVIRI AODs ($r = 0.92$), suggesting that to first order, the influence of variable surface conditions and dust height have been successfully accounted for. As expected, the presence of dust acts to reduce the OLR resulting in a LW warming of the Earth-atmosphere system as a whole. In the SW at TOA the situation is more complicated: here peak daytime heating of the Earth-atmosphere tends to be comparable to that seen in the LW, but there are periods of dust induced SW cooling toward dawn and dusk. Figure 7 illustrates this more clearly by showing the mean daytime cycle in AOD (a), TOA dust DRE (b), SFC dust DRE (c), and dust radiative flux divergence (d). Figure 7b clearly shows a strong daytime cycle in DRE_{SWTOA} and DRE_{LWTOA}, with both peaking toward local noon and hence reinforcing each other in the net effect. Conversely, toward dawn and dusk, the dust induced SW cooling counteracts the smaller LW heating at this time and can result in an overall cooling of

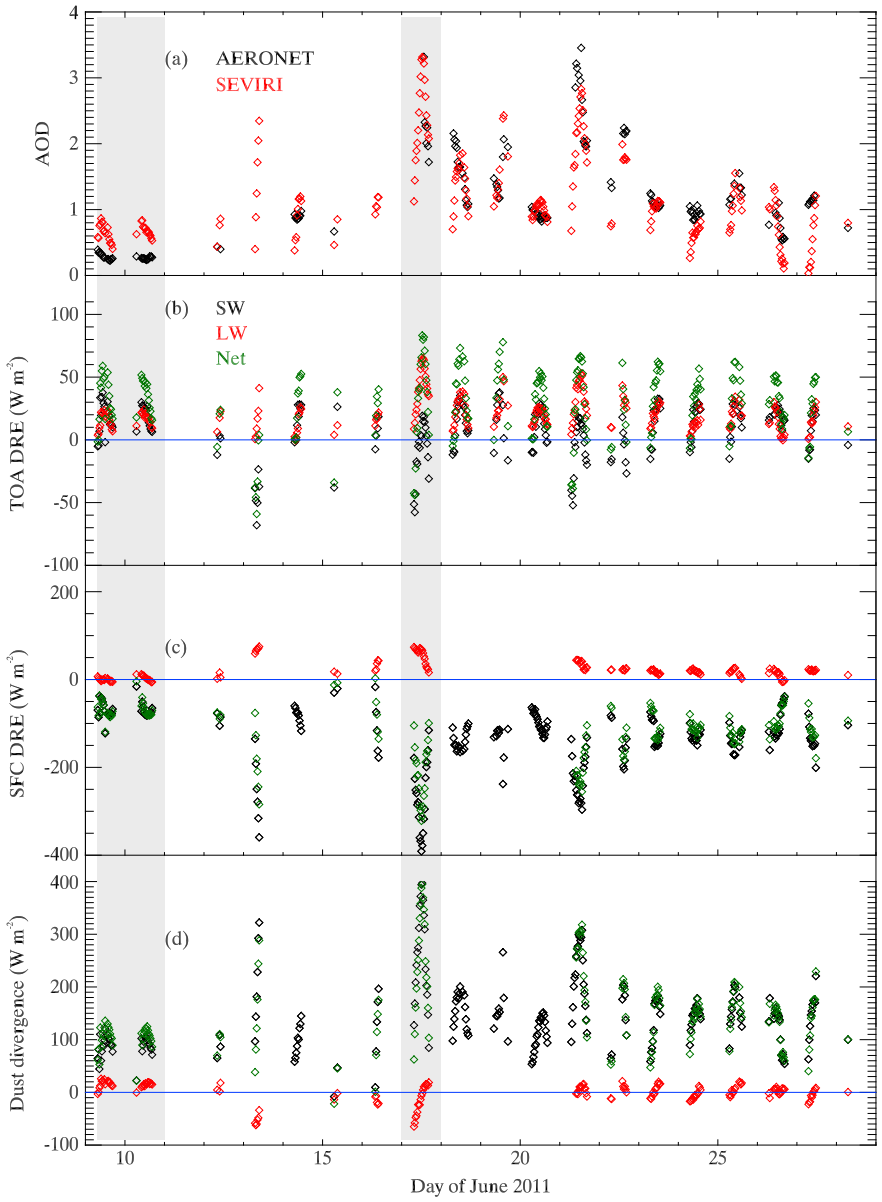

Figure 5. Timeseries of (a) AOD at 550 nm from AERONET and SEVIRI, (b) TOA DRE, (c) SFC DRE from surface FT measurements, and (d) Atmospheric radiative divergence due to dust. Data are available from 0700 to 1630 UTC each day and are plotted for co-located AODs, TOA DREs, and FT fluxes. FT temperature measurements are not available for 14 and 18–20 June; hence, there are no DRE_{LWSFC} retrievals nor LW dust divergences on these days.

the Earth-atmosphere system. This behavior does not appear to be due to any systematic daytime cycle in AOD (Figure 7a) but is consistent with the findings of *Ansell et al.* [2014] who showed observationally that it is easier to obtain an overall SW cooling when the Sun is at a higher solar zenith angle. They argue that for a given AOD, the behavior of the DRE_{SWTOA} is governed by the dependence of the pristine-sky albedo and directional dust scattering on solar zenith angle. While the former effect alone would see a relative heating by dust as solar zenith angle increases, in this case, the second effect appears to be dominating, backscatter fraction from the dust layer increasing with solar zenith such that cooling occurs when the Sun is close to the horizon. Similar theoretical results were obtained by *Russell et al.* [1997] whose simulations over ocean showed that for a given AOD, the change in the total reflected SW flux as a function of time of day is expected to be greatest when the solar zenith angle is at an intermediately high level, early in the morning or late in the afternoon.

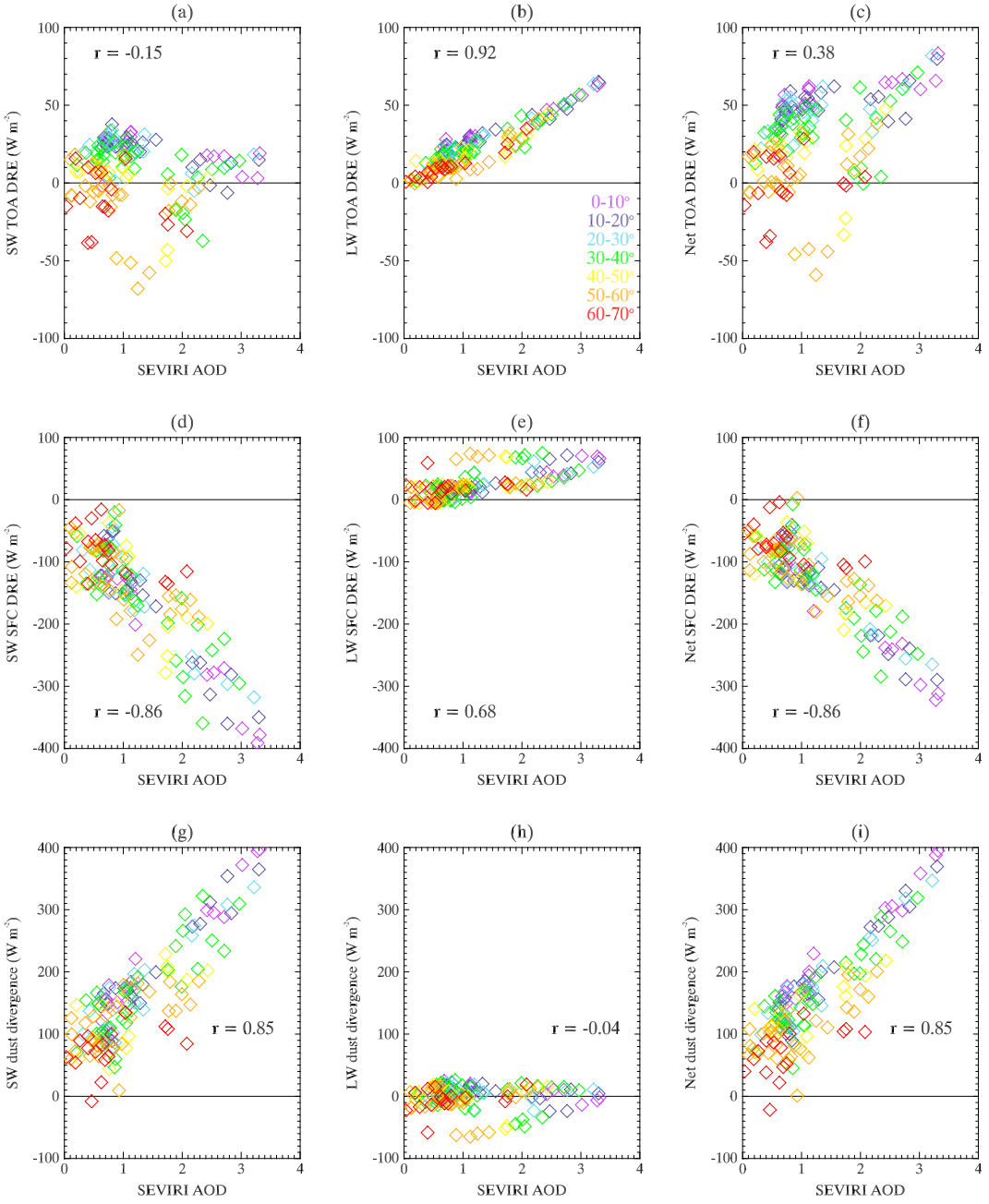

Figure 6. Scatterplots of SW, LW, and net dust DREs with respect to SEVIRI AOD, for (a,b,c) TOA, (d,e,f) surface, and (g,h,i) atmospheric dust divergence. Points are color-coded by solar zenith angle.

At the surface, the increased sensitivity of SW fluxes to the presence of dust relative to its effect at the TOA noted in section 3.1 is confirmed with strong surface SW cooling seen at the highest dust loads (Figure 5c). This is confirmed by Figure 6(d) which clearly shows the very high anticorrelation of −0.86 between the SW surface heating and the SEVIRI AOD. This is a result of two factors: (i) the relatively small contrast between surface and planetary albedo over BBM and (ii) SW absorption within the dust layer itself which reinforces the effects of dust backscatter in reducing the SW radiation reaching the surface. Estimates of the dust single scattering albedo, ω_0, from the AERONET measurements give an average value of 0.977 at 675 nm over the period studied here, indicating that while the dust is predominantly scattering some absorption is occurring. We note here that any inability of the AERONET measurements to capture the effects of larger dust particles will also likely bias ω_0 high [*Ryder et al.*, 2013a]. In the LW the presence of dust tends to warm the

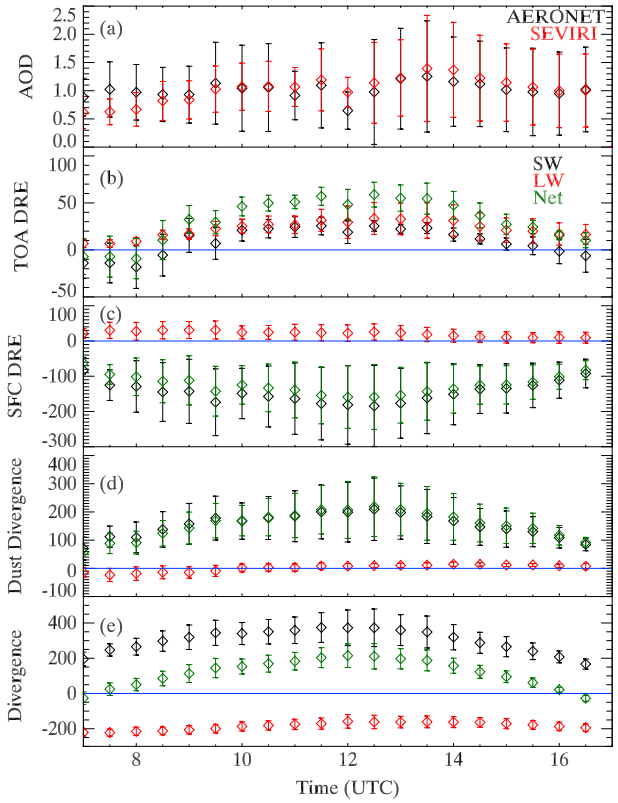

Figure 7. Daytime cycle in mean: (a) AOD from co-located SEVIRI (red) and AERONET (black), (b) TOA DRE, (c) SFC DRE, (d) Atmospheric radiative divergence due to dust, and (e) Total atmospheric radiative divergence. Figures 7b–7d have units of W m^{-2}. Error bars indicate the standard deviation in the mean value.

surface through enhanced downward emission from the dust layer itself. Overall, through the daytime, the reduction in downwelling SW radiation tends to dominate such that significant atmospheric dust loading leads to an overall net radiative surface cooling. Compared to the measurements at TOA, there is a slightly different daytime cycle in DRE_{SWSFC} and DRE_{LWSFC}, with maximum cooling in the SW in the middle of the day (mean cooling of ~180 W m^{-2}). The magnitude of this cycle is rather larger than at TOA. Meanwhile maximum heating in the LW occurs shortly after dawn but the overall pattern is different to at TOA, with DRE_{LWSFC} values slowly decreasing over the course of the day from ~50 W m^{-2} to ~25 W m^{-2}. The daytime cycle of the net effect follows that of the SW effect.

Combining the TOA and surface response to dust allows its impact on the radiative divergence of the atmospheric column to be discerned. Because of the relative magnitude of the SW TOA and SFC DREs, it is the surface term that dominates the overall radiative impact of dust on the atmospheric column, resulting in a SW radiative heating (Figure 5d) which is highly correlated to dust loading (Figure 6g). Toward local noon, the surface and TOA effects act in the same direction, augmenting the heating effect whereas toward dusk and dawn the SW TOA cooling noted earlier reduces the overall SW heating. In general however, in the SW, dust always acts to warm the atmosphere (Figure 7d). In the LW during the daytime, the radiative impact of dust is such that it enhances atmospheric cooling by heating the surface but reduces cooling to space. The latter has a more pronounced daytime signature, with a slight asymmetry reflecting the lag in the daytime cycle of surface temperature relative to peak insolation (Figure 7b). Overall, the surface and the TOA effects balance each other in the LW, with a very slight mean cooling during the month of −0.1 W m^{-2}, while the instantaneous values of $LW_{divdust}$ range from −65 to +26 W m^{-2}. The magnitude of this cooling is relatively small, only becoming significant in terms of its contribution to the net atmospheric radiative divergence in the early morning when the LW impact of dust at the TOA is minor. Overall, this means that the presence of dust through the daytime results in a net radiative heating of the atmosphere, which attains maximum values between ~1100 and 1330 UTC over the BBM site. Note that at BBM local noon is at ~1150 UTC. On the daytime average, given the negligible LW contribution noted above, over BBM during June 2011 the radiative divergence due to dust is controlled by the SW mean heating of 153 W m^{-2}.

The episodic nature of dust events is confirmed by the variability in the dust radiative effects, variability which peaks in the middle of the day when the dust atmospheric heating is strongest (as can be seen from the standard deviation error bars in Figure 7d). Between 1100 and 1300 UTC, dominated by the SW cooling of the surface by dust, the net dust divergence ranges from ~100 to 390 W m^{-2} between light and heavy dust event days, respectively. Note that even on light dust days, there is a nonnegligible atmospheric heating due to dust, which reinforces the point that dust is an ever-present feature of the environment around BBM during June 2011.

How significant is this dust radiative heating of the atmosphere in the context of the total clear-sky atmospheric radiative divergence? Figure 7e shows the mean daytime cycle seen in this latter field for the SW

and LW components and the overall net (recall that observations are only included when the scene is not identified as cloudy by SEVIRI). Comparing the divergences from Figures 7d and 7e shows that in the SW dust plays a key role in determining the overall clear-sky SW heating, comprising of the order 50% of the total SW divergence. In the LW, while the mean dust radiative divergence is typically less than 20 W m^{-2} in magnitude and can change sign through the day (Figure 7c), the corresponding clear-sky divergence is consistently of the order −190 W m^{-2} (Figure 7d). Clearly another atmospheric constituent, presumably water vapor, dominates the daytime atmospheric LW behavior, resulting in strong LW radiative cooling throughout the day. The different patterns of LW and SW behavior mean that the atmospheric net radiative heating due to dust alone typically exceeds the total net clear-sky radiative heating. Because the LW radiative cooling of the atmosphere becomes relatively more significant toward dusk and dawn, the total clear-sky net divergence implies atmospheric cooling at these times (Figures 7d and 4d). Conversely, the dust-only net divergence always shows heating, being controlled by the SW component. Given the ubiquitous nature of dust over the site, it is clear that dust, via its influence on SW radiation, plays a major role in determining the mean clear-sky radiative heating over the site during this period.

3.3. Consequences of Temporal Sampling

The mean temporal behavior illustrated in Figure 7 has interesting implications for estimates of dust radiative effects from instruments in polar orbit. As discussed by *Kocha et al.* [2013], there are consequences for climatologies of dust presence if there is insufficient diurnal sampling. Over the BBM site for the particular month studied, we have seen that there is no obvious coherent daytime signal in atmospheric dust loading (Figure 7a). However, the time-dependent signatures seen in the TOA dust DRE (Figure 7b), which propagate through to the atmospheric radiative divergence (Figure 7d), appear more dependent on solar geometry, via the level of solar insolation and dust backscatter dependence, and the daily surface temperature cycle.

Instruments such as CERES [*Wielicki et al.*, 1996] on satellites in polar orbit, such as NASA's Aqua and EUMETSAT's MetOp satellites, are limited to, at most, only two overpasses over a specific location per day: for Aqua, the BBM daytime overpass time ranges from ~1230–1330 UTC. These timeslots are more generally applicable to all instruments onboard NASA's A-Train series of satellites. From Figure 7b, it is apparent that instruments in the A-train would thus be sampling a time when the TOA DRE indicates a strong dust induced warming: on average, the TOA DRE is 24 W m^{-2} in the SW and 32 W m^{-2} in the LW between 1230 and 1330 UTC, as opposed to 8 W m^{-2} in the SW and 21 W m^{-2} in the LW when averaged across 0700-1630 UTC. Considering only dust radiative effects evaluated near local noon as representative of daytime values in these type of environments (desertic, moderate-high surface albedo) will thus systematically bias estimates of the net daytime dust DRE high by missing both the cooling SW effect and the reduced LW heating effect seen toward sunset and sunrise.

4. Conclusions

The availability of ground-based measurements at Bordj Badji Mokhtar has permitted, for the first time, quantitative observation-based estimates of the radiative effects of dust at the surface, TOA, and within the atmosphere for the central Sahara. Although substantial in global terms, the high dust loadings seen over BBM in June 2011 were not exceptional for this region, and hence, the results seen may be taken as broadly representative for the site at this time of year.

In common with studies of other aerosol species over a variety of different scenes [e.g., *Podgorny et al.*, 2000], the observations over BBM indicate that dust radiative impacts are, in general, significantly more pronounced at the surface than at the TOA. This behavior is particularly apparent in the SW, with dust induced instantaneous reductions in downwelling surface SW fluxes reaching over 300 W m^{-2}. In contrast, the similarity between the characteristics of the uplifted dust and the underlying desert surface mean that the corresponding impact on TOA SW fluxes is of the order 5–10 times smaller. In the LW, surface and TOA dust effects are more equivalent—of the order 10s W m^{-2}—although the former still tend to have a larger magnitude. More crucially for the overall net impact, through the majority of the day at the TOA, the SW and LW effects act in the same direction, heating the Earth-atmosphere system as a whole. Under heavy dust loadings (AOD at 550 nm > 3), the net dust DRE at the TOA can thus reach values of over 80 W m^{-2} near local noon. Conversely, at the surface, enhanced downward LW emission from the dust layer partially counteracts the reduction in downward SW fluxes. For the largest AODs recorded during the period considered here, the net radiative cooling of the surface is reduced by up to 75 W m^{-2} due to this increase in LW emission.

Considering the time-resolved behavior of the dust radiative effect in more detail, there are distinct daytime cycles in dust impact at both the TOA and at the surface, although for the latter the absolute values are more significant. At the TOA, given the lack of an obvious coherent temporal behavior in dust loading, it appears that the effects of the daytime cycle in solar insolation are key. In the LW, it would appear that this influence is felt principally via surface temperature, with an enhanced contrast between emission from the surface and that from the dust layer occurring when surface temperature reaches its peak value. Dust top height will also have a role to play, but previous studies indicate that, certainly for local uplift, a more extended dust layer might be expected to develop through the morning toward local noon as solar heating helps turbulent mixing from the surface to become established [e.g., *Knippertz et al.*, 2009]. In the SW, two competing effects come into play, both acting as a function of solar zenith angle. While the pristine-sky planetary albedo increases with solar zenith, the backscatter fraction from the dust layer itself is also enhanced. From the results seen, it appears that the second effect is dominant such that SW TOA cooling frequently occurs toward dawn and dusk. This time-varying nature of the TOA DRE is manifested in the mean daily cycle with mean net TOA DRE values ranging from $-9\,W\,m^{-2}$ in the morning to $59\,W\,m^{-2}$ in the middle of the day. Meanwhile at the surface, the presence of a thick dust layer tends to have the greatest absolute cooling effect in the SW in the middle of the day but the greatest cooling effect relative to the incoming solar flux at either end of the day. This is a consequence of the increased backscatter off the top of the dust layer at higher solar zenith angles and the increased path length through the dust layer. In the LW, dust layers have a greater ability to warm the surface early in the morning than at the end of the day, indicative of the contrast in the diurnal cycle of surface and lower atmospheric temperatures.

Unifying the measurements made at TOA and the surface, we can draw some conclusions about the impact of dust on the atmosphere alone. Here we see that the LW cooling caused by dust plays a relatively minor role compared to the SW heating of the atmosphere, except at the beginning of the day when there is more equivalence between the two components. Across the day, the mean SW heating of the atmosphere is of the order $150\,W\,m^{-2}$ while the corresponding LW cooling is negligible. Over the period studied, the net dust radiative heating peaks at $390\,W\,m^{-2}$. Hence, while at TOA the LW impact of dust is substantial and similar in significance to the SW impact, in the atmosphere itself the effect in the LW is much less important. This difference in SW and LW dust impact is broadly consistent with results presented by *Sicard et al.* [2014] and is simply a reflection of the opposing effects that the two components have at the surface, modified by the relatively smaller effect of dust on both components at the TOA. Overall then, during the daytime dust has a net radiative warming effect on the atmosphere, which reduces in magnitude toward dawn and dusk. The day to day variability in the net atmospheric radiative warming due to dust is dominated by the variability in net radiative effect at the surface. Near noon, when the maximum net atmospheric radiative heating is seen, the surface net DRE varies between -322 and $-53\,W\,m^{-2}$ in comparison to a variation of between 17 and $83\,W\,m^{-2}$ in TOA net DRE. Through comparison with the total net radiative divergence of the atmosphere, we find that the net atmospheric radiative heating due to dust is substantially offset by atmospheric LW cooling, most likely due to water vapor.

Given our developing understanding of the subdaily patterns of dust activity in the region, we can now make some assessments as to the radiative impacts of various types of dust events. Events associated with the breakdown of the low-level jet (LLJ) typically occur between around 0800–0900 UTC [e.g., *Washington et al.*, 2006; *Marsham et al.*, 2013], by which time there is sufficient potential for atmospheric radiative heating (by over $\sim 100\,W\,m^{-2}$). There is a less consistent diurnal pattern in the arrival of cold pool events, but often they will occur overnight, at which time we can speculate that the dust would enhance atmospheric radiative cooling, both by heating the surface and, dependent on the development of a nocturnal temperature inversion, potentially enhancing TOA LW emission. However, mixing in the deep daytime boundary layer ensures that dust lofted by both mechanisms can have long atmospheric residence times of over a day, so while the initial radiative impact of LLJ events will therefore be different from that of cold pool events, the longer term impacts will be similar.

The temporal behavior that we have identified over BBM indicates the need to fully account for the direct and indirect effects of solar geometry and, to a lesser extent, coherence in dust variability to accurately diagnose overall daytime dust radiative effects. In particular, estimates of DRE_{NetTOA} would be biased high if midday measurements were used as representative of the true daytime mean, an issue which could propagate into elevated estimates of dust atmospheric radiative heating. Looking forward, a complete analysis of the effects of dust throughout the diurnal cycle would be of substantial scientific interest. The LW

component of Figures 7b–7d implies slight net atmospheric radiative cooling at night dominated by heating of the surface, especially during the latter stages of the night. To test such a hypothesis would require the provision of dust loading estimates through the night: work is ongoing to extend the SEVIRI AOD retrieval algorithm to include nighttime retrievals. Such a resource will allow us to establish the full significance of the LW effects of dust on the Earth's radiative energy budget and to characterise the overall net impact of the different types of dust events.

Acknowledgments

We would particularly like to thank Azzedine Saci, Abdelkader Ouladichir, Bouziane Ouchene, and Mohammed Salah-Ferroudj of the Office National de la Météorologie of Algeria (ONM) for managing and running the Fennec supersite at BBM, and Benyakoub Abderrahmane, Mohammmed Limam, and Diali Sidali (ONM) for their assistance. Further thanks is due to all the members of the Fennec ground-based field campaign team and especially to Martin Todd (University of Sussex) for access to the AERONET data. The Royal Meteorological Institute of Belgium provided the GERB HR data used in the DRE retrievals. The MODIS emissivity data product was obtained through the online Data Pool at the NASA Land Processes Distributed Active Archive Center (LP DAAC). The ERA-Interim meteorological data used in the AOD and DRE_{LWTOA} retrievals were produced by ECWMF, and access to the data set was provided by the British Atmospheric Data Centre. The SEVIRI AOD and DRE data used in this study are processed and archived at Imperial College London; contact Jamie Banks (j.banks@imperial.ac.uk) for more details and to request data access. Research reported in this publication has been supported by the King Abdullah University of Science and Technology (KAUST). Finally, we would like to thank the three anonymous reviewers and the editor for their valuable comments which greatly improved this paper.

References

Allan, R. P., M. J. Woodage, S. F. Milton, M. E. Brooks, and J. M. Haywood (2011), Examination of long-wave radiative bias in general circulation models over North Africa during May–July, *Q. J. R. Meteorol. Soc.*, *137*, 1179–1192, doi:10.1002/qj.717.

Allen, C. J. T., R. Washington, and S. Engelstaedter (2013), Dust emission and transport mechanisms in the central Sahara: Fennec ground-based observations from Bordj Badji Mokhtar, June 2011, *J. Geophys. Res. Atmos.*, *118*, 6212–6232, doi:10.1002/jgrd.50534.

Anderson, G. P., et al. (2000), MODTRAN4: Radiative transfer modeling for remote sensing, in *Algorithms for Multispectral, Hyperspectral, and Ultraspectral Imagery VI*, edited by S. S. Chen, and M. R. Descour, *Proc. SPIE Int. Soc. Opt. Eng.*, *4049*, 176–183, Orlando, Fla., doi:10.1117/12.410338.

Ansell, C., H. E. Brindley, Y. Pradhan, and R. Saunders (2014), Mineral dust aerosol net direct radiative effect during GERBILS field campaign period derived from SEVIRI and GERB, *J. Geophys. Res. Atmos.*, *119*, 4070–4086, doi:10.1002/2013JD020681.

Ansmann, A., A. Petzold, K. Kandler, I. Tegen, M. Wendisch, D. Müller, B. Weinzierl, T. Müller, and J. Heintzenberg (2011), Saharan Mineral Dust Experiments SAMUM-1 and SAMUM-2: What have we learned?, *Tellus B*, *63*, 403–429, doi:10.1111/j.1600-0889.2011.00555.x.

Ashpole, I., and R. Washington (2012), An automated dust detection using SEVIRI: A multi-year climatology of summertime dustiness in the central and western Sahara, *J. Geophys. Res.*, *117*, D08202, doi:10.1029/2011JD016845.

Banks, J. R., and H. E. Brindley (2013), Evaluation of MSG-SEVIRI mineral dust retrieval products over North Africa and the Middle East, *Remote Sens. Environ.*, *128*, 58–73, doi:10.1016/j.rse.2012.07.017.

Banks, J. R., H. E. Brindley, C. Flamant, M. J. Garay, N. C. Hsu, O. V. Kalashnikova, L. Klüser, and A. M. Sayer (2013), Intercomparison of satellite dust retrieval products over the west African Sahara during the Fennec campaign in June 2011, *Remote Sens. Environ.*, *136*, 99–116, doi:10.1016/j.rse.2013.05.003.

BouKaram, D., C. Flamant, P. Knippertz, O. Reitebuch, P. Pelon, M. Chong, and A. Dabas (2008), Dust emissions over the Sahel associated with the West African Monsoon inter-tropical discontinuity region: A representative case study, *Q. J. R. Meteorol. Soc.*, *134*(632), 621–634, doi:10.1002/qj.244.

Brindley, H. E. (2007), Estimating the top-of-atmosphere longwave radiative forcing due to Saharan dust from satellite observations over a west African surface site, *Atmos. Sci. Lett.*, *8*, 74–79, doi:10.1002/asl.155.

Brindley, H. E., and J. E. Russell (2009), An assessment of Saharan dust loading and the corresponding cloud-free longwave direct radiative effect from geostationary satellite observations, *J. Geophys. Res.*, *114*, D23201, doi:10.1029/2008JD011635.

Christopher, S. A., J. Wang, Q. Ji, and S.-C. Tsay (2003), Estimation of diurnal shortwave dust aerosol radiative forcing during PRIDE, *J. Geophys. Res.*, *108*(D19), doi:10.1029/2002JD002787.

Clerbaux, N., S. Dewitte, L. Gonzalez, C. Bertrand, B. Nicula, and A. Ipe (2003), Outgoing longwave flux estimation: Improvement of angular modelling using spectral information, *Remote Sens. Environ.*, *85*(3), 389–395, doi:10.1016/S0034-4257(03)00015-4.

Dee, D. P., et al. (2011), The ERA-Interim reanalysis: Configuration and performance of the data assimilation system, *Q. J. R. Meteorol. Soc.*, *137*, 553–597, doi:10.1002/qj.828.

Derrien, M., and H. L. Gléau (2005), MSG/SEVIRI cloud mask and type from SAFNWC, *Int. J. Remote Sens.*, *26*(21), 4707–4732, doi:10.1080/01431160500166128.

Dewitte, S., L. Gonzalez, N. Clerbaux, A. Ipe, C. Bertrand, and B. D. Paepe (2008), The Geostationary Earth Radiation Budget Edition 1 data processing algorithms, *Adv. Space Res.*, *41*, 1906–913, doi:10.1016/j.asr.2007.07.042.

Dubovik, O., B. Holben, T. F. Eck, A. Smirnov, Y. J. Kaufman, M. D. King, D. Tanré, and I. Slutsker (2002), Variability of absorption and optical properties of key aerosol types observed in worldwide locations, *J. Atmos. Sci.*, *59*, 590–608, doi:10.1175/1520-0469(2002)059<0590:VOAAOP>2.0.CO;2.

Eck, T. F., B. N. Holben, J. S. Reid, O. Dubovik, A. Smirnov, N. T. O'Neill, I. Slutsker, and S. Kinne (1999), Wavelength dependence of the optical depth of biomass burning, urban, and desert dust aerosols, *J, Geophys. Res.*, *104*(D24), 31,333–31,349, doi:10.1029/1999JD900923.

Engelstaedter, S., I. Tegen, and R. Washington (2006), North African dust emissions and transport, *Earth Sci. Rev.*, *79*, 73–100, doi:10.1016/j.earscirev.2006.06.004.

Garcia-Carreras, L., J. H. Marsham, D. J. Parker, C. L. Bain, S. Milton, A. Saci, M. Salah-Ferroudj, B. Ouchene, and R. Washington (2013), The impact of convective cold pool outflows on model biases in the Sahara, *Geophys. Res. Lett.*, *40*, 1647–1652, doi:10.1002/grl.50239.

Harries, J. E., et al. (2005), The geostationary earth radiation budget project, *Q. J. R. Meteorol. Soc.*, *86*, 945–960, doi:10.1175/BAMS-86-7-945.

Haywood, J. M., P. N. Francis, M. D. Glew, and J. P. Taylor (2001), Optical properties and direct radiative effect of saharan dust: A case study of two Saharan dust outbreaks using aircraft data, *J. Geophys. Res.*, *106*(D16), 18,417–18,430, doi:10.1029/2000JD900319.

Haywood, J. M., R. P. Allan, I. Culverwell, T. Slingo, S. Milton, J. Edwards, and N. Clerbaux (2005), Can desert dust explain the outgoing longwave radiation anomaly over the Sahara during July 2003?, *J. Geophys. Res.*, *110*, D05105, doi:10.1029/2004JD005232.

Haywood, J. M., et al. (2011), Motivation, rationale and key results from the GERBILS Saharan dust measurement campaign, *Q. J. R. Meteorol. Soc.*, *137*, 1106–1116, doi:10.1002/qj.797.

Highwood, E. J., J. M. Haywood, M. D. Silverstone, S. M. Newman, and J. P. Taylor (2003), Radiative properties and direct effect of Saharan dust measured by the C-130 aircraft during Saharan Dust Experiment (SHADE): 2. Terrestrial spectrum, *J. Geophys. Res.*, *108*(D18), 8578, doi:10.1029/2002JD002552.

Hobby, M., et al. (2013), The Fennec Automatic Weather Station (AWS) Network: Monitoring the Saharan climate system, *J. Atmos. Oceanic Technol.*, *30*(4), 709–724, doi:10.1175/JTECH-D-12-00037.1.

Holben, B. N., et al. (1998), AERONET—A federated instrument network and data archive for aerosol characterization, *Remote Sens. Environ.*, *66*(1), 1–16, doi:10.1016/S0034-4257(98)00031-5.

Hsu, N. C., J. R. Herman, and C. Weaver (2000), Determination of radiative forcing of Saharan dust using combined TOMS and ERBE data, *J. Geophys. Res.*, *105*(D16), 20,649–20,661, doi:10.1029/2000JD900150.

Knippertz, P., and M. C. Todd (2012), Mineral dust aerosols over the Sahara: Meteorological controls on emission and transport and implications for modeling, *Rev. Geophys.*, *50*, RG1007, doi:10.1029/2011RG000362.

Knippertz, P., J. Trentmann, and A. Seifert (2009), High-resolution simulations of convective cold pools over the northwestern Sahara, *J. Geophys. Res.*, *114*, D08110, doi:10.1029/2008JD011271.

Kocha, C., P. Tulet, J.-P. Lafore, and C. Flamant (2013), the importance of the diurnal cycle of aerosol optical depth in West Africa, *Geophys. Res. Lett.*, *40*, 785–790, doi:10.1002/grl.50143.

Lensky, I. M., and D. Rosenfeld (2008), Clouds-Aerosols-Precipitation Satellite Analysis Tool (CAPSAT), *Atmos. Chem. Phys.*, *8*, 6739–6753, doi:10.5194/acp-8-6739-2008.

Loeb, N. G., N. Manalo-Smith, S. Kato, W. F. Miller, S. K. Gupta, P. Minnis, and B. A. Wielicki (2003), Angular distribution models for top-of-atmosphere radiative flux estimation from the clouds and the earths radiant energy system instrument on the tropical rainfall measuring mission satellite. Part I: Methodology, *J. Appl. Meteorol.*, *42*(2), 240–265, doi:10.1175/1520-0450(2003)042<0240:ADMFTO>2.0.CO;2.

Marsham, J. H., D. J. Parker, C. M. Grams, C. M. Taylor, and J. M. Haywood (2008), Uplift of Saharan dust south of the intertropical discontinuity, *J. Geophys. Res.*, *113*, D21102, doi:10.1029/2008JD009844.

Marsham, J. H., P. Knippertz, N. S. Dixon, D. J. Parker, and G. M. S. Lister (2011), The importance of the representation of deep convection for modeled dustłgenerating winds over West Africa during summer, *Geophys. Res. Lett.*, *38*, L16803, doi:10.1029/2011GL048368.

Marsham, J. H., et al. (2013), Meteorology and dust in the central Sahara: Observations from Fennec supersite-1 during the June 2011 intensive observation period, *J. Geophys. Res. Atmos.*, *118*, 4069–4089, doi:10.1002/jgrd.50211.

McFarlane, S. A., E. I. Kassianov, J. Barnard, C. Flynn, and T. P. Ackerman (2009), Surface shortwave aerosol radiative forcing during the atmospheric radiation measurement mobile facility deployment in Niamey, Niger, *J. Geophys. Res.*, *114*, D00E06, doi:10.1029/2008JD010491.

Milton, S. F., G. Greed, M. E. Brooks, J. Haywood, B. Johnson, R. P. Allan, A. Slingo, and W. M. F. Grey (2008), Modeled and observed atmospheric radiation balance during the West African dry season: Role of mineral dust, biomass burning aerosol, and surface albedo, *J. Geophys. Res.*, *113*, D00C02, doi:10.1029/2007JD009741.

Ogawa, K., T. Schmugge, and S. Rokugawa (2008), Estimating broadband emissivity of arid regions and its seasonal variations using thermal infrared remote sensing, *IEEE Trans. Geosci. Remote Sens.*, *46*(2), 334–343, doi:10.1109/TGRS.2007.913213.

Podgorny, I. A., W. Conant, V. Ramanathan, and S. K. Satheesh (2000), Aerosol modulation of atmospheric and surface solar heating over the tropical Indian Ocean, *Tellus B*, *52*(3), 947–958, doi:10.1034/j.1600-0889.2000.d01-4.x.

Prospero, J. M., P. Ginoux, O. Torres, S. E. Nicholson, and T. E. Gill (2002), Environmental characteristics of global sources of atmospheric soil dust identified with the Nimbus 7 Total Ozone Mapping Spectrometer (TOMS) absorbing aerosol product, *Rev. Geophys.*, *40*(1), 1002, doi:10.1029/2000RG000095.

Quijano, A. L., I. N. Sokolik, and O. B. Toon (2000), Radiative heating rates and direct radiative forcing by mineral dust in cloudy atmospheric conditions, *J. Geophys. Res.*, *105*(D10), 12,207–12,219, doi:10.1029/2000JD900047.

Ricchiazzi, P., S. Yang, C. Gautier, and D. Sowle (1998), SBDART: A research and teaching software tool for plane-parallel radiative transfer in the earth's atmosphere, *Bull. Am. Meteorol. Soc.*, *79*(10), 2101–2114, doi:10.1175/1520-0477(1998)079<2101:SARATS>2.0.CO;2.

Rodwell, M. J., and T. Jung (2008), Understanding the local and global impacts of model physics changes: An aerosol example, *Q. J. R. Meteorol. Soc.*, *134*, 1479–1497, doi:10.1002/qj.298.

Russell, P. B., S. A. Kinne, and R. W. Bergstrom (1997), Aerosol climate effects: Local radiative forcing and column closure experiments, *J. Geophys. Res.*, *102*(D8), 9397–9407, doi:10.1029/97JD00112.

Ryder, C. L., et al. (2013a), Optical properties of Saharan dust aerosol and contribution from the coarse mode as measured during the Fennec 2011 aircraft campaign, *Atmospheric Chemistry and Physics*, *13*, 303–325, doi:10.5194/acp-13-303-2013.

Ryder, C. L., E. J. Highwood, T. M. Lai, H. Sodemann, and J. H. Marsham (2013b), Impact of atmospheric transport on the evolution of microphysical and optical properties of Saharan dust, *Geophys. Res. Lett.*, *40*, 2433–2438, doi:10.1002/grl.50482.

Schepanski, K., I. Tegen, M. C. Todd, B. Heinold, G. Bönisch, B. Laurent, and A. Macke (2009), Meteorological processes forcing Saharan dust emission inferred from MSG-SEVIRI observations of subdaily dust source activation and numerical models, *J. Geophys. Res.*, *114*, D10201, doi:10.1029/2008JD010325.

Schmetz, J., P. Pili, S. Tjemkes, D. Just, J. Kerkmann, S. Rota, and A. Ratier (2002), An introduction to Meteosat Second Generation (MSG), *Bull. Am. Meteorol. Soc.*, *83*, 977–992, doi:10.1175/1520-0477(2002)083<0977:AITMSG>2.3.CO;2.

Sicard, M., S. Bertolín, M. Mallet, P. Dubuisson, and A. Comerón (2014), Estimation of mineral dust long-wave radiative forcing: Sensitivity study to particle properties and application to real cases in the region of Barcelona, *Atmos. Chem. Phys.*, *14*, 9213–9231, doi:10.5194/acp-14-9213-2014.

Slingo, A., et al. (2006), Observations of the impact of a major Saharan dust storm on the atmospheric radiation balance, *Geophys. Res. Lett.*, *33*, L24817, doi:10.1029/2006GL027869.

Slingo, A., H. E. White, N. A. Bharmal, and G. J. Robinson (2009), Overview of observations from the RADAGAST experiment in Niamey, Niger: 2. Radiative fluxes and divergences, *J. Geophys. Res.*, *14*, D00E04, doi:10.1029/2008JD010497.

Todd, M. C., et al. (2013), Meteorological and dust aerosol conditions over the western Saharan region observed at Fennec supersite-2 during the intensive observation period in June 2011, *J. Geophys. Res. Atmos.*, *118*, 8426–8447, doi:10.1002/jgrd.50470.

Tompkins, A. M., C. Cardinali, J.-J. Morcrette, and M. Rodwell (2005), Influence of aerosol climatology on forecasts of the African Easterly Jet, *Geophys. Res. Lett.*, *32*, L10801, doi:10.1029/2004GL022189.

Wang, J., S. A. Christopher, J. S. Reid, H. Maring, D. Savoie, B. N. Holben, J. M. Livingston, P. B. Russell, and S.-K. Yang (2003), GOES 8 retrieval of dust aerosol optical thickness over the Atlantic Ocean during PRIDE, *J. Geophys. Res.*, *108*(D19), 8595, doi:10.1029/2002JD002494.

Wang, Z., M. Barlage, X. Zeng, R. E. Dickinson, and C. B. Schaaf (2005), The solar zenith angle dependence of desert albedo, *Geophys. Res. Lett.*, *32*, L05403, doi:10.1029/2004GL021835.

Washington, R., M. C. Todd, S. Engelstaedter, S. Mbainayel, and F. Mitchell (2006), Dust and the low-level circulation over the Bodélé Depression, Chad: Observations from BoDEx 2005, *J. Geophys. Res.*, *111*, D03201, doi:10.1029/2005JD006502.

Washington, R., et al. (2012), Fennec—The Saharan climate system, *CLIVAR Exchanges*, *60*(17), 31–33.

Wielicki, B. A., B. R. Barkstrom, E. F. Harrison, R. B. Lee, G. L. Smith, and J. E. Cooper (1996), Clouds and the Earth's Radiant Energy System (CERES): An earth observing system experiment, *Bull. Am. Meteorol. Soc.*, *77*(5), 853–868, doi:10.1175/1520-0477(1996)077<0853:CATERE>2.0.CO;2.